

# Deuterium-deuterium fusion charged particle detection using CR-39 and Deep Learning Model

Yuxing Wang <sup>a</sup>, Allan Xi Chen <sup>a\*</sup>, Matthew Salazar <sup>b</sup>, Nawar Abdalla <sup>b</sup>, Zhifei Li <sup>b</sup>,  
Benjamin Wrixon <sup>b</sup>

Alpha Ring International Limited

<sup>a</sup> 1631 W. 135<sup>th</sup> St. Gardena, CA 90249, U.S.A.

<sup>b</sup> 5 Harris Ct. Building B, Monterey, CA 93940, U.S.A.

## Abstract

CR-39 solid-state nuclear track detectors are widely used in fusion research for detecting charged particles produced in fusion reactions. However, analyzing increasingly complex and large-scale CR-39 track images to extract meaningful information can be a tedious and time-consuming process, often prone to human errors and bias. To address these challenges, we developed an AI-based classification model capable of differentiating protons, tritons, and helions produced during D-D fusion, using CR-39 track images as input data. The CR-39 track images were processed and used to train a deep learning model. By preprocessing the track images for noise reduction and feature enhancement, we trained the YOLOv8 [1][2] network to distinguish the three particle types with high accuracy. The proposed model achieved a classification accuracy of over 96%, demonstrating its potential for improving automated track analysis in CR-39 detectors. Additionally, the model precisely identifies particle coordinates and counts, enabling comprehensive particle analysis. This study highlights the application of AI in track detection and classification, offering a robust solution for particle identification in CR-39 detector-based experiments.

Keywords: YOLOv8; CR-39; SSNTD; AI Fusion; Deep Learning Image Classification

## 1. Introduction

In fusion energy research, solid-state nuclear track detectors (SSNTD) like Columbia Resin #39 (CR-39) offer a robust and interference-resistant method for identifying charged particles from deuterium-deuterium (D-D) and proton-Boron11 (p-B11) fusion reactions[3] In this study, CR-39 detectors were used in conjunction with an Alpha Ring compact ion beam system (ARI-IBS) [4] to analyze particle tracks produced during D-D fusion. Figure 1 illustrates the experimental setup and image acquisition process, which includes chemical etching and high-resolution imaging using the TASL TASTRAK system--an advanced image acquisition system specifically designed for analyzing SSNTDs.

Previous studies have encountered challenges related to background impurities in the CR-39 processing workflow and the potential for repeated recognition of particles due to coupon partitioning. The research explored methods such as refining the particle labeling process and implementing data preprocessing techniques. However, a residual

\* Corresponding author e-mail address: [allan@alpharing.com](mailto:allan@alpharing.com) (Allan Xi Chen)

error rate of approximately 9% persisted [5]. To address the issue of particle detection along coupon slice edges, our study noted that due to the small and densely packed particles, multiple parameter adjustments were attempted but yielded suboptimal results. As a solution, the original large-scale images were segmented to ensure that small particles were represented with sufficient resolution, followed by scaling to the standard YOLOv8 input size of 640×640. This approach effectively reduced particle density within a single image. Furthermore, an overlapping tiling strategy was employed to prevent particles from being split across tiles. Overlapping regions were incorporated during the segmentation process to ensure that each particle was entirely captured in at least one tile. To mitigate duplicate detections in overlapping regions, the Intersection over Union (IoU) metric was utilized, with a threshold of 0.5. IoU is a measure of the overlap between the predicted and ground truth bounding boxes, calculated as the ratio of their intersection area to their union area, providing an evaluation of detection accuracy. Detections exceeding this threshold were merged into a single detection, with the bounding box having the highest confidence retained as the final detection. This methodology aimed to improve detection accuracy and ensure more reliable identification of particles in densely packed regions.

Our study focuses on utilizing these CR-39 tracks to train a deep learning model capable of particle classification, position annotation, and quantity estimation. This automated approach overcomes challenges posed by overlapping tracks and varying track characteristics, providing a scalable and efficient method.

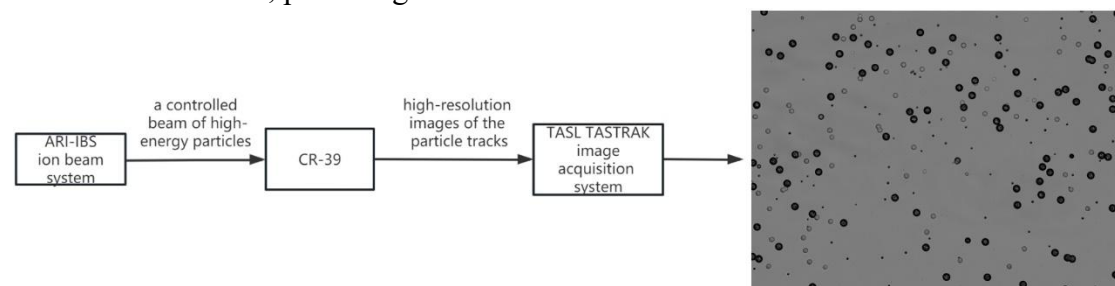


Figure 1: CR-39 Particle Track Detection with ARI-IBS Ion Beam System and TASTRAK Imaging.

## 2. Methods

The overall flowchart for data processing and model training for D-D Fusion particle detection using Deep Learning Model, is shown in figure 2 below. The object detection pipeline begins with input processing, where the raw data is preprocessed for optimal feature extraction. The Backbone, based on CSPDarknet, extracts multi-level features using Cross Stage Partial (CSP) structures, enhancing gradient flow and reducing computational complexity. These features are then passed to the Neck, implemented as Path Aggregation Network (PANet), which aggregates multi-scale information to preserve fine details crucial for accurate object localization. The Head, utilizing an anchor-free approach, directly predicts object locations without predefined anchor boxes, improving detection flexibility and efficiency. In the post-processing stage, Non-Maximum Suppression (NMS) and confidence filtering refine the detections by removing redundant or low-confidence predictions. Finally, the optimized model is exported for deployment, ready for real-world applications in various environments.

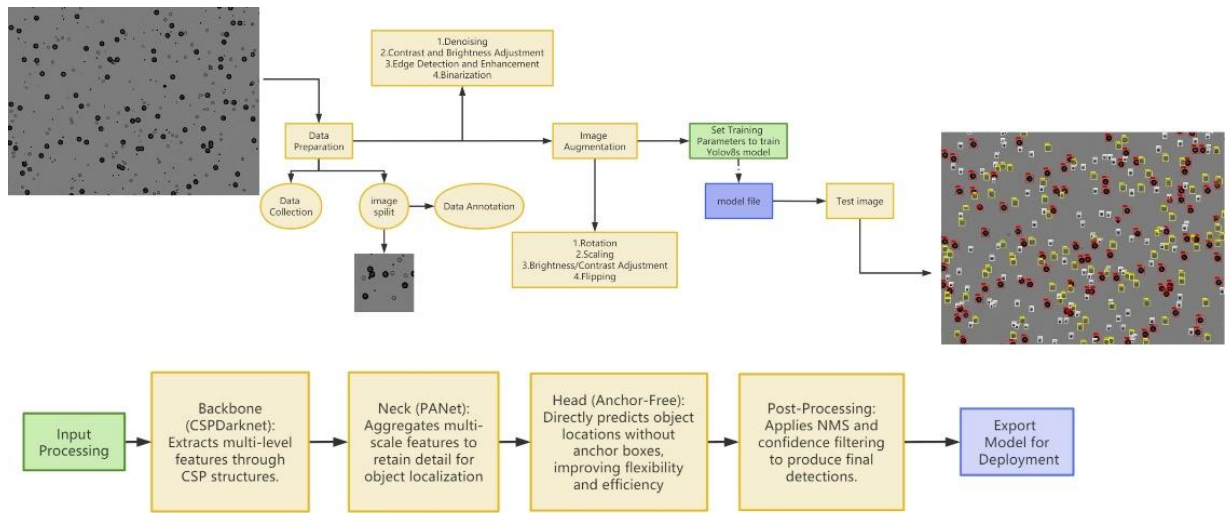


Figure 2: Flowchart for data processing and model training for D-D fusion particle detection using deep learning model

## 2.1. Data Processing

High-resolution images of measurable nuclear tracks were obtained during D-D fusion experiments conducted under controlled conditions using the ARI-IBS. For training, 90 images with a resolution of  $409 \times 384$  pixels were processed, while 10 images with the same resolution were reserved for validation. The images containing valid tracks of the three types of particles were confirmed by ARI experiment personnel and used to construct the dataset. Additionally, an independent test set consists of 231 images with a resolution of  $2048 \times 1538$  pixels. The raw images were divided into smaller blocks to reduce memory usage, improve computational efficiency, enhance local feature detection, minimize noise interference, and enable more detailed regional analysis. Each particle track was labeled as a proton, triton, or helion using the LabelImg tool to create the training and validation dataset. Subsequently, preprocessing steps, including denoising, contrast enhancement, and normalization, were applied to improve feature clarity and optimize the data for model training.

## 2.2. Model Training

In this study, the YOLOv8 model was employed for detecting and classifying CR-39 track images, utilizing an NVIDIA RTX A2000 GPU with 12 GB of memory to enhance computational efficiency and accelerate inference. The hardware and software configuration information is provided in the table below. The model processes input images by normalizing and resizing them to a fixed resolution before feeding them into the CSPDarknet backbone, which extracts hierarchical features such as edges, textures, and object shapes. CSPDarknet is a variant of the Darknet architecture that incorporates Cross-Stage Partial (CSP) connections to enhance gradient flow, reduce computational redundancy, and improve feature learning efficiency. CSP connections achieve this by splitting the feature map into two parts, processing one part through transformations while keeping the other unchanged, and then merging them, effectively reducing

duplicate computation and enhancing the network's representation capability and inference speed.[6] The extracted features are further refined through the Path Aggregation Network (PANet) in the Neck module, enabling multi-scale feature fusion that enhances the detection of small, medium, and large objects. PANet is an extension of the Feature Pyramid Network (FPN) that modifies the original top-down feature pyramid by introducing a bottom-up path augmentation, lateral connections, and adaptive pooling. The bottom-up path augmentation reconstructs feature hierarchies by adding an additional pathway that transfers low-level spatial details back to higher levels. Lateral connections integrate features between adjacent layers to maintain consistency across scales, while adaptive pooling helps aggregate global context information for more robust feature representation. The detection Head adopts an anchor-free design, directly predicting object locations and classes, which improves flexibility and eliminates the need for predefined anchor boxes. Unlike anchor-based methods that rely on predefined box priors, anchor-free approaches predict object centers, offsets, and scales directly from feature maps, reducing computational complexity and enhancing adaptability to varying object scales and aspect ratios. In the post-processing stage, Non-Maximum Suppression (NMS) eliminates redundant bounding boxes and filters predictions based on confidence scores, ensuring accurate and non-redundant detections. NMS is an algorithm used in object detection to retain the most relevant bounding box by suppressing those with high overlap (IoU) while keeping the one with the highest confidence score. YOLOv8's key innovations, including multi-scale feature fusion and an anchor-free design, significantly enhance its capability to detect complex and overlapping track structures across diverse scenarios. The model is benefit from the parallel processing capabilities of the GPU, enabling real-time detection with optimized memory utilization and accelerated tensor operations through CUDA and TensorRT, making it highly efficient for large-scale data processing. [7][8][9]

To evaluate the model's performance, metrics including precision, recall, F1-score, and mean average precision (mAP) were utilized. These metrics comprehensively assess the accuracy of particle classification, the detection of overlapping particles, and the model's robustness under varying particle density conditions. The metrics are as follows:

$$\text{Precision} = \frac{\text{TP}}{\text{TP} + \text{FP}} \quad (1)$$

$$\text{Recall} = \frac{\text{TP}}{\text{TP} + \text{FN}} \quad (2)$$

$$\text{F1-Score} = 2 \cdot \frac{\text{Precision} \cdot \text{Recall}}{\text{Precision} + \text{Recall}} \quad (3)$$

$$\text{Mean Average Precision (mAP)} = \frac{1}{N} \sum_{i=1}^N \text{AP}_i \quad (4)$$

$$\text{AP} = \int_0^1 \text{Precision}(\text{Recall}) d(\text{Recall}) \quad (5)$$

In object detection evaluation, TP (True Positives) refers to instances where the model correctly identifies an object as belonging to the target class. FP (False Positives)

occurs when the model incorrectly identifies an object. FN (False Negatives) represents cases where the model fails to detect an object that actually exists, missing it entirely. Additionally,  $AP_i$  (Average Precision for class  $i$ ) quantifies the model's performance for a specific class by calculating the area under the Precision-Recall curve for that class. Precision measures the proportion of correctly identified positive samples among all predicted positives, while Recall reflects the model's ability to detect all relevant objects. F1-Score balances Precision and Recall, particularly for imbalanced classes. Average Precision (AP) represents the area under the Precision-Recall curve and Mean Average Precision (mAP) averages AP across all classes, providing a comprehensive measure of detection performance. Together, these metrics evaluate the model's accuracy, completeness, and reliability. The inference times averaged 361 MS per image.

Table 1: Hardware and Software Configuration for AI training

Hardware		Software	
GPU Model	NVIDIA RTX A2000	NVIDIA-SMI Version	552.23
GPU Memory	12 GB	Driver Version	552.23
Pytorch Version	2.5.0	CUDA Version	12.4
Yolo Version	v8s	Python Version	3.12

### 2.1. Post-Training Validation

After training, the model was rigorously evaluated on a separate set of CR-39 images that were not used during the training or validation phases. These test images consisted of high-resolution data with varying particle densities, captured at different reaction times (45, 90, and 180 minutes). As shown from the Post Training Validation of the Result (Manual Counting vs Model Counting) below, we assess the model's performance from manual counting by experts served as a benchmark, ensuring accurate particle classification, precise localization, and count reliability. This process involved manually identifying and categorizing particles within each image, carefully comparing the model's predictions with the expert-verified counts. Particular attention was given to detecting overlapping tracks, accurately distinguishing between particle types, and verifying the total particle counts within each image. The manual annotations vs. AI model annotations for particle detection in microscopy are shown below (Fig.3).

Table 2: Training and validation of results (manual counting vs. AI model counting)

image	Manual Counting (5 images)					Model Counting (5 images)					Accur acy
	1	2	3	4	5	1	2	3	4	5	total
triton	92	93	83	103	106	93	94	87	106	108	98%
helion	67	91	83	96	106	66	91	82	96	104	99%
proton	85	105	107	78	90	87	108	109	80	94	97%

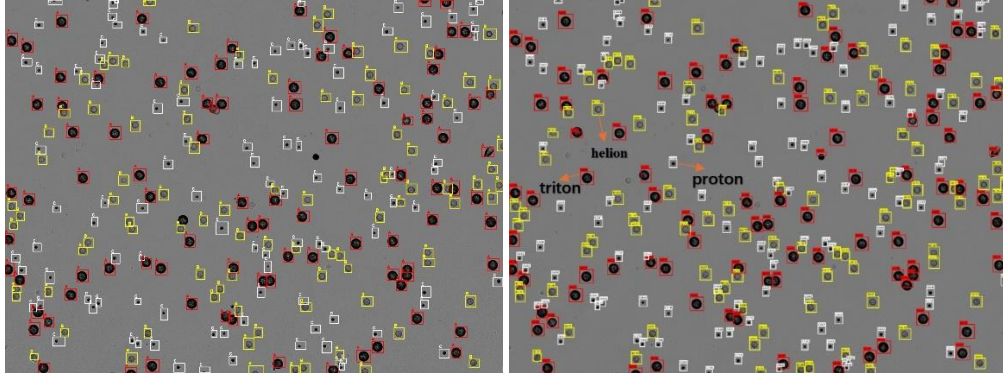


Figure 3: Manual annotations of image1 (Left) vs. AI model annotations of image 1 (Right) for particle detection.

#### 2.4. Model Application

The trained YOLOv8 model was integrated into a user-friendly graphical user interface (GUI) to facilitate automated analysis of CR-39 images (Fig. 4). The GUI is designed with an intuitive layout, divided into upper and lower sections. This interface supports single-image and batch processing, displaying labeled images alongside real-time particle counts. The original image is displayed on the left, while the processed image with labeled particles and bounding boxes is shown on the right. The interface also displays the quantities of each particle type and the total particle count in real time. When a folder is selected, images are processed one by one, and the outputs include processed/labeled image files and CSV summaries of particle classifications and coordinates. The CSV file contains the filename, particle classifications, bounding box coordinates for each particle, counts of each particle type, and the total particle count. The coordinates output by YOLOv8 represents the bounding box positions within the input image, measured in pixels. They include the top-left corner ( $x_{min}$ ,  $y_{min}$ ) and the bottom-right corner ( $x_{max}$ ,  $y_{max}$ ), defining the boundaries of the detected object. These coordinates are absolute values relative to the resized input image dimensions. The bounding box coordinates from the detection results are transformed back to the full-image coordinate system to ensure accurate placement on the original image, while allowing data in overlapping regions to be overwritten for consistency. Subsequently, Non-Maximum Suppression (NMS) is applied to remove redundant detections in overlapping areas, merging all results and drawing the final bounding boxes on the original image. This process effectively resolves issues of missed

detections at image boundaries, ensuring the completeness and accuracy of the detection results. For folder uploads, the CSV file also includes a summary of the total particle statistics for all processed images. This GUI system streamlines the workflow from image input to results output, enabling efficient and automated analysis of CR-39 images, significantly improving the accuracy and speed of the detection method.

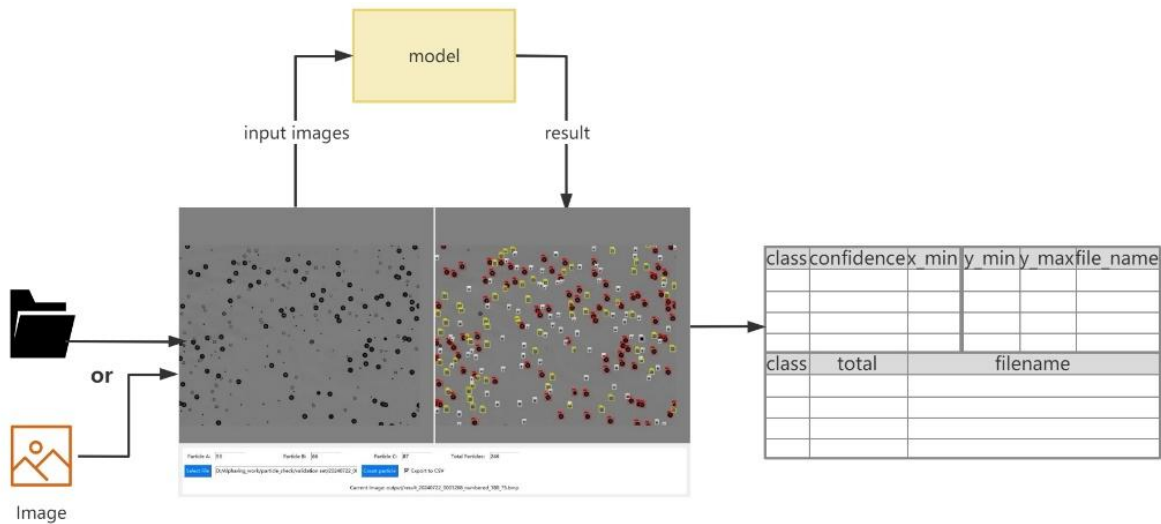


Figure 4: CR39 Particle detection and classification pipeline: from image input to exporting the results.

### 3. Results

The combined F1-score (Fig. 5) reaches its peak value of 0.91 at an optimal confidence threshold of 0.383, achieving a balance between precision and recall. This threshold provides robust performance across all particle classes, making it the most suitable choice for real-world applications in CR-39 particle detection and classification.

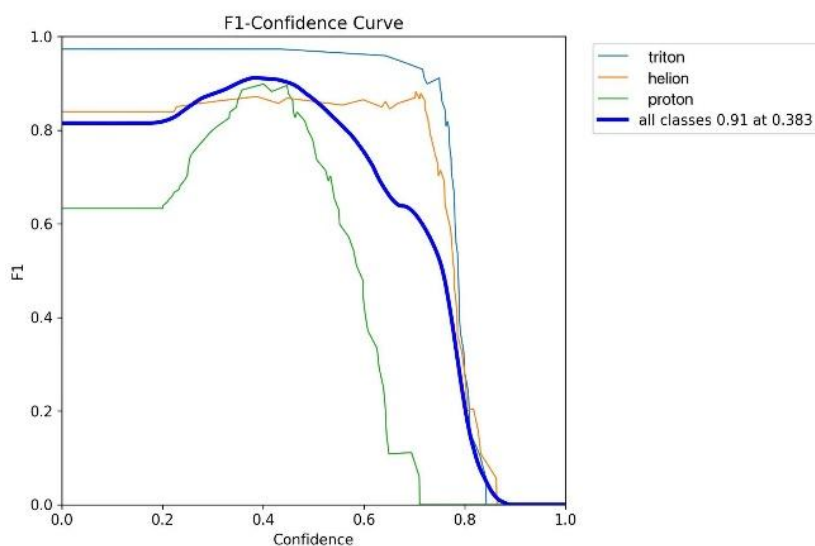


Figure 5: F1-Confidence Curve

The Precision-Confidence Curve (Fig. 6) shows that Class triton achieves the highest precision across most confidence thresholds, while Class proton exhibits greater

fluctuation, indicating higher classification difficulty. For all classes combined, the maximum precision of 1.00 is achieved at a confidence threshold of 0.843. The Precision-Recall Curve (Fig. 7) highlights the trade-off between precision and recall, with triton achieving the best performance (AP = 0.983), followed by helion (AP = 0.920) and proton (AP = 0.880). The overall mean average precision (mAP) for all classes is 0.928 at an IoU threshold of 0.5. The Recall-Confidence Curve (Fig. 8) demonstrates that Class triton maintains a high recall across a wide range of thresholds, while proton shows a significant drop in recall at higher confidence levels. These metrics collectively confirm the model's robustness and effectiveness in CR-39 particle detection and classification tasks.

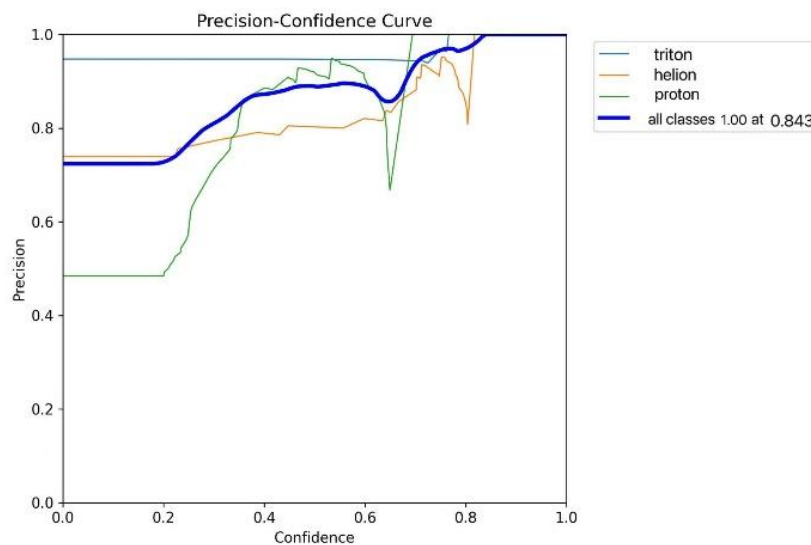


Figure 6: Precision-Confidence Curve

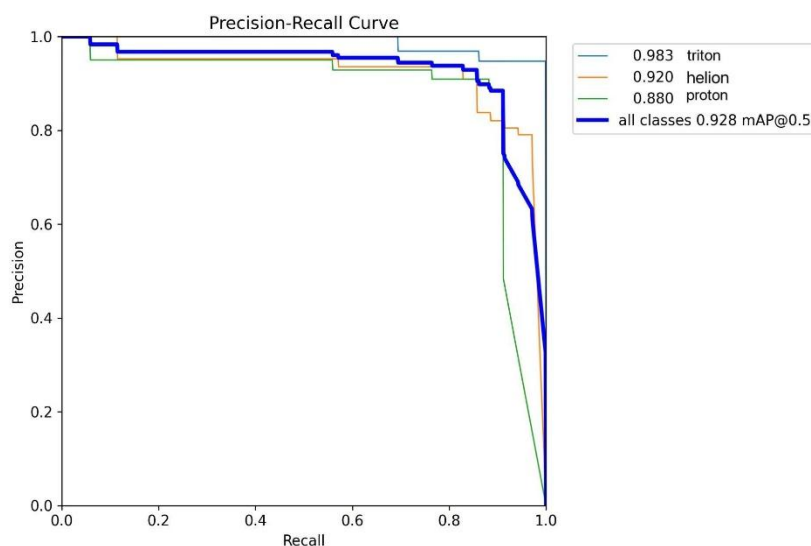


Figure 7: Precision-Recall Curve



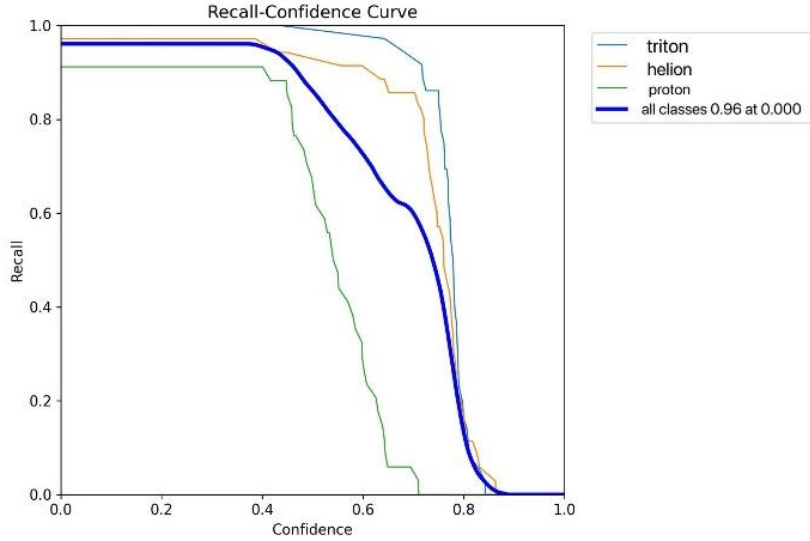


Figure 8: Recall-Confidence Curve

The training losses (including box loss, classification loss, DFL loss, and validation losses) are presented in figure 9. All loss curves show a consistent downward trend, demonstrating that the model is effectively learning, and the optimization process is stable. For helions, the precision and recall metrics exhibit a steady improvement throughout the training process, with both metrics nearing and exceeding 90%, indicating strong detection performance for this class. Additionally, the mAP50 and mAP50-95 metrics display an upward trend, confirming the model's ability to generalize across various IoU thresholds. The smooth convergence of the loss curves, coupled with the rising evaluation metrics, underscores the robustness and reliability of the model training process.

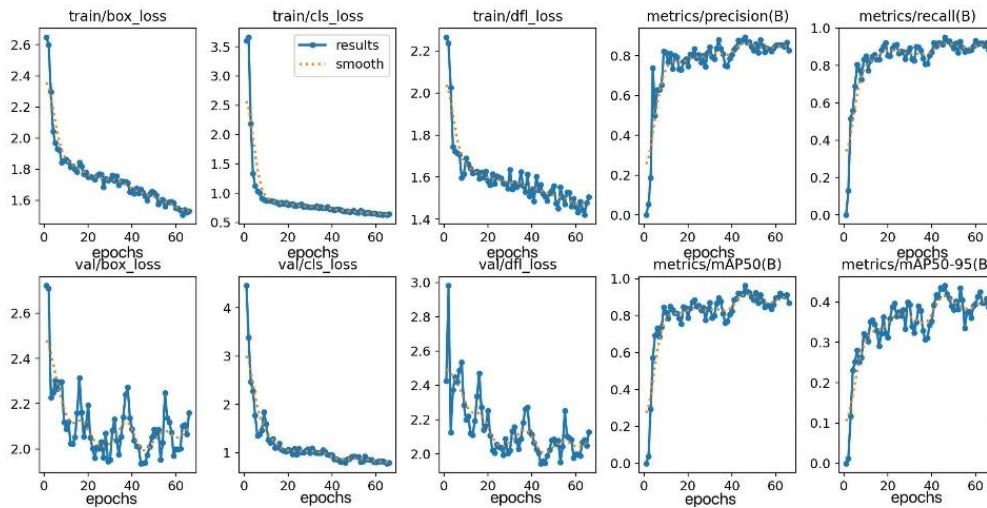


Figure 9: Loss curves and evaluation metrics

### 3.1. Background Noise

To assess the model's robustness against background noise, we conducted detection experiments using 20 images containing only background noise as a control group. The results indicate that in 13 out of 20 images, the model did not detect any particles,

demonstrating its effectiveness in filtering out background noise. However, in 7 images, the model incorrectly identified particles, misclassifying background impurities as actual particles. This suggests that while the model is generally effective in suppressing background noise, certain complex noise patterns may still lead to occasional false positives. Observations show that most noise particles are misclassified as helion particles. Since helion particles are more abundant and have distinct features, the model tends to predict them more frequently. Additionally, the similarity in shape between helion particles and certain background noise features has led to misclassification. As illustrated in figure 10, both images belong to the background noise control group. The left image shows no detected particles, highlighting the model’s capability to eliminate the influence of background noise. In contrast, the right image exhibits a single false positive detection, representing a minor misclassification case. These findings indicate that although the model demonstrates strong noise suppression, further improvements—such as enhanced data preprocessing and stricter confidence thresholds—may be necessary to minimize misidentifications caused by background artifacts.

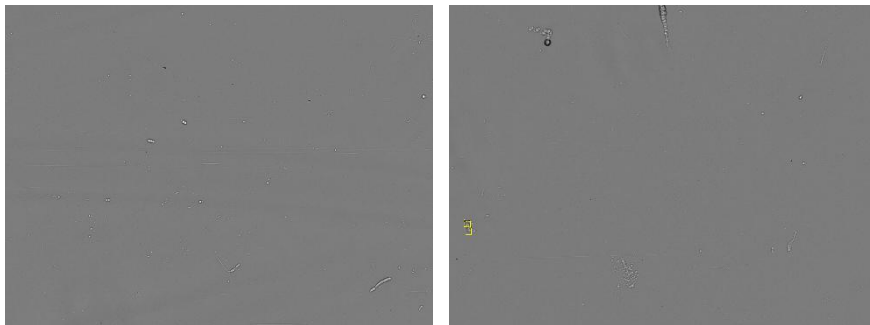


Figure 10: Blank CR39 coupon for background noise control. (Left) Noise eliminated vs. (right) minor false detection.

Table 3: Sample detection results for 20 blank coupons to assess the background noise.

	Triton	Helion	Proton	#Total
1	0	0	0	0
2	0	0	0	0
3	0	0	0	0
4	0	0	0	0
5	0	0	0	0
6	0	0	0	0
7	0	1	0	1
8	1	0	0	1
9	0	0	0	0
10	0	1	0	1
11	0	0	0	0
12	0	2	0	2
13	0	0	0	0

14	0	1	0	1
15	0	0	0	0
16	0	0	0	0
17	0	0	0	0
18	1	0	0	1
19	0	0	0	0
20	0	2	0	2

### 3.2. Comparison with ImageJ Analysis

As shown in the Fig.11, the conventional ImageJ method can identify particles but struggles to separate overlapping ones and classify different types. The process involves pixel-to-physical size conversion, 8-bit grayscale conversion, and thresholding (0-80 pixel values as particles, the rest as background). The image is then converted into a binary mask with black background and white particles, followed by particle analysis that filters out excessively large, small, or non-circular particles to reduce misidentifications. However, ImageJ is limited in handling overlapping particles, often merging them into a single detection or filtering them out entirely, and is sensitive to background noise. While ImageJ allows particle counting, it struggles to distinguish different types due to variations in size and brightness.

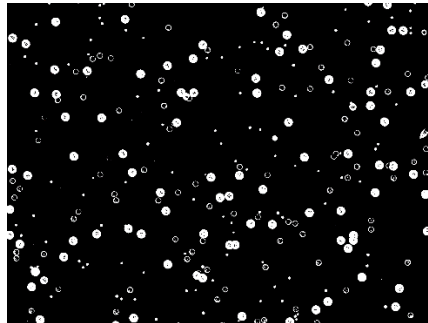


Figure 11: Traditional image processing using ImageJ for particle recognition.

YOLOv8, based on deep learning, overcomes some of these limitations by automatically adapting to different particle detectors and experimental conditions without manual parameter adjustments. It can handle variations in particle shape, size, density, and lighting conditions, making it more robust for complex detection tasks. Furthermore, GPU parallel processing significantly accelerates inference speed, achieving real-time detection in milliseconds. Unlike ImageJ, YOLOv8 eliminates the need for manual intervention, reducing subjective errors and enhancing both detection accuracy and efficiency, making it a more scalable solution for CR-39 particle analysis.

## 4. Conclusion

In this study, we utilize the computational power of GPUs to enhance the efficiency of YOLOv8 model training. When processing an identical task involving 100 images, the training time on a CPU is observed to be 1 hour, whereas the same task is

completed in 0.062 hours (approximately 3.7 minutes) on a GPU. This substantial reduction in training time underscores the superior parallel processing capabilities of GPUs, which facilitates a significant improvement in computational efficiency and resource utilization. The inherent architecture of GPUs, with their high core count and parallel processing capabilities, allows for the simultaneous execution of multiple operations, thereby accelerating training processes and enabling the efficient handling of large-scale datasets. Consequently, the adoption of GPU-based training offers a substantial advantage in terms of both time efficiency and scalability, making it a preferred choice for high-performance deep learning applications.

The trained YOLOv8 model demonstrates significant potential for real-world applications, particularly in automating CR-39 particle detection and classification processes. This is especially valuable for analyzing beam energy-dependent yields in D-D and eventually p-B11 fusion reactions. By correlating particle classification results with energy spectra, the model validates energy calibration and attenuation effects through accurate particle-type identification and localization. Its applicability extends to STEM education, where integrating the model into automated analysis pipelines offers students a hands-on opportunity to efficiently interpret data, deepening their understanding of nuclear diagnostics and particle detection without the complexity of manual data processing.

Future work could focus on expanding the dataset, especially for challenging cases like protons, incorporating more advanced architecture such as transformers or ensemble methods to improve performance, and optimizing the model for deployment in resource-constrained environments. Additionally, adapting the model for other particle detection tasks or broader applications in nuclear diagnostics could further enhance its utility. This work provides a foundation for leveraging deep learning in automated CR-39 image analysis, opening new opportunities for advancing research and education in nuclear science.

## **5. Acknowledgement**

The authors would like to thank Prof. Roger Falcone, Prof. Richard Petrasso, Prof. Jyhpyng Wang, Dr. Kosta Yanev, Dr. Nathan Eschbach, Mr. Iskren Vankov, Mr. Christian Yoo, Mr. Peter Liu, Mr. Paul Chau, Ms. Belinda Mei, Dr. Peter Hsieh, Mr. Wilson Wu, and Mr. Charles Wu for valuable discussion and insight. This work was conducted by scientists and engineers as employees of Alpha Ring International Limited and its affiliated companies. This study was funded by Alpha Ring International Limited, which supports the education and training of a fusion industry workforce. The funding from Alpha Ring International Limited did not influence the scientific integrity or the results of this study.

## 6. References

- [1]. Jocher, G., Qiu, J., & Chaurasia, A. (2023). Ultralytics YOLO (Version 8.0.0) [Computer software]. <https://github.com/ultralytics/ultralytics>
- [2]. Redmon, J., Divvala, S., Girshick, R., & Farhadi, A. (2016). You only look once: Unified, real-time object detection. In *Proceedings of the IEEE conference on computer vision and pattern recognition* (pp. 779-788).
- [3]. J. Charvát, F. Spurný The (DD) fusion reaction products identification using the CR 39 track detector *Int. J. Radiat. Appl. Instrum. Nucl. Tracks Radiat. Meas.*, 19 (1–4) (1991), pp. 585-590, [10.1016/1359-0189\(91\)90272-J](https://doi.org/10.1016/1359-0189(91)90272-J)
- [4]. Chen, Allan Xi, Nai-Wei Liu, Alexander Gunn, Zhe Su, Benjamin F. Sigal, Matthew Salazar, Nawar Abdalla, James Chen, Alfred Y. Wong, and Qiong Wang. "Compact Ion Beam System for Fusion Demonstration." *\*Physics Open\** 21 (2024): 100234. <https://doi.org/10.1016/j.physo.2024.100234>.
- [5]. H. Xu, et. Al., Automatic counting method for alpha tracks on CR-39 detectors based on the YOLOv8 image recognition algorithm  
doi:10.13140/RG.2.2.34051.82724
- [6]. C. -Y. Wang, H. -Y. Mark Liao, Y. -H. Wu, P. -Y. Chen, J. -W. Hsieh and I. -H. Yeh, "CSPNet: A New Backbone that can Enhance Learning Capability of CNN," 2020 IEEE/CVF Conference on Computer Vision and Pattern Recognition Workshops (CVPRW), Seattle, WA, USA, 2020, pp. 1571-1580, doi: 10.1109/CVPRW50498.2020.00203.
- [7]. Chen, Jinming, Qiliang Du and Lianfang Tian. "Surface Defect Detection Algorithm Based on Improved YOLOv8 Model." *2023 4th International Conference on Intelligent Computing and Human-Computer Interaction (ICHCI)* (2023): 382-386.
- [8]. R. Varghese and S. M., "YOLOv8: A Novel Object Detection Algorithm with Enhanced Performance and Robustness," *2024 International Conference on Advances in Data Engineering and Intelligent Computing Systems (ADICS)*, Chennai, India, 2024, pp. 1-6, doi: 10.1109/ADICS58448.2024.10533619.bb
- [9]. Liu, Moyun, Youping Chen, Jingming Xie, Lei He and Yang Zhang. "LF-YOLO: A Lighter and Faster YOLO for Weld Defect Detection of X-Ray Image." *IEEE Sensors Journal* 23 (2021): 7430-7439.